Nanoscale

COMMUNICATION

View Article Online
View Journal | View Issue

Cite this: *Nanoscale*, 2026, **18**, 5168

Received 12th November 2025,
Accepted 29th January 2026

DOI: 10.1039/d5nr04783h

rsc.li/nanoscale

Cu–Ag tandem electrodes with controlled Ag overlayer thickness for tunable CO_2 reduction

Yojiro Kimura[a] and Miho Yamauchi *[a,b,c,d]

Tandem catalysts that integrate a CO-selective metal such as Ag with C–C coupling-active Cu represent a promising strategy to tailor product selectivity for electrochemical CO_2 reduction (eCO_2R). Here, we fabricated Cu–Ag tandem electrodes (Cu–Ag TEs) with an Ag overlayer with thicknesses precisely controlled from 0.9 to 150 nm *via* physical vapor deposition on a porous polytetrafluoroethylene (PTFE) membrane. We systematically investigated how nanometer-scale thickness modulation affects product selectivity under flow-cell conditions. Electrocatalytic tests revealed a non-monotonic dependence of product selectivity on the Ag thickness. Methane (CH_4) formation, scarcely observed on monometallic Cu or Ag, was substantially enhanced and peaked at an Ag overlayer thickness of approximately 10 nm. In contrast, C_{2+} selectivity decreased with increasing Ag thickness up to 10 nm and then increased again at larger thicknesses. *In situ* Raman spectroscopy detected a Raman peak assignable to $*CH_x$–*CO intermediates, suggesting a thickness-dependent competition between the $*CH_x$–*CO and $*CH_x$–*H pathways. These findings demonstrate that Ag overlayer thickness and the resulting interfacial structure serve as tunable parameters for controlling eCO_2R selectivity in Cu–Ag TEs.

Introduction

Electrochemical CO_2 reduction reaction (eCO_2R) powered by renewable energy has attracted increasing attention as a promising route for the sustainable conversion of CO_2 into value-added products.[1–3] Among various metal catalysts, copper (Cu) is uniquely capable of catalyzing C–C coupling, enabling the formation of multicarbon products (C_{2+}) such as ethylene (C_2H_4) and ethanol (EtOH).[1,4–7] However, eCO_2R proceeds through many competing pathways, yielding broad product distributions.[6,8] Achieving high selectivity for a targeted product remains a central challenge for practical implementation.[3]

To address this issue, tandem catalyst designs that combine C–C coupling-active Cu with a CO-selective metal such as Ag, Au, or Zn have been proposed as a strategy to enhance selectivity.[9–12] In the tandem architectures, *CO generated on the non-Cu metal can migrate to the Cu surface, thereby increasing local *CO coverage and promoting C–C coupling.[6,9,10,13–15] For example, Cu–Ag tandem catalysts promote the formation of C_{2+} *via* *CO–*CO coupling[11,16] and improve the ethanol-to-ethylene ratio *via* $*CH_x$–*CO coupling.[2,17,18]

In previous studies, most Cu–Ag tandem catalysts were prepared by sequential/mixed deposition of Cu and Ag particles,[11–13,17,18] or by modifying Cu nanoparticles with Ag.[15,16,19] The former approach often results in poorly defined and inhomogeneous metal–metal interfaces, while the latter makes it difficult to precisely and systematically control the Ag loading at the nanoscale. As a result, it has been difficult to understand how interfacial design influences intermediate transport and downstream product selectivity.

In this study, we address these limitations by constructing Cu–Ag tandem electrodes (Cu–Ag TEs) in which the Ag overlayer thickness is precisely controlled using physical vapor deposition (PVD), while maintaining a constant Cu thickness. Unlike conventional gas-diffusion-layer (GDL) supports, we use a porous PTFE membrane as the substrate, because we previously found that the membrane suppresses the hydrogen evolution reaction (HER) when used for Cu deposition.[20] This design allows reliable evaluation of eCO_2R performance in a flow cell configuration at high current density, while minimizing interference from HER. These features collectively enable a

[a]*Mitsui Chemicals, Inc., Carbon Neutral Energy Research Center (MCI–CNRC), International Institute for Carbon-Neutral Energy Research (I²CNER), Kyushu University, 744 Motooka, Nishi-ku, Fukuoka-shi, Fukuoka, 819-0395, Japan*
[b]*Institute for Materials Chemistry and Engineering (IMCE), Kyushu University, Motooka 744, Nishi-ku, Fukuoka 819-0395, Japan.*
E-mail: yamauchi@ms.ifoc.kyushu-u.ac.jp
[c]*Research Center for Negative Emissions Technologies (K-NETs), Kyushu University, Motooka 744, Nishi-ku, Fukuoka 819-0395, Japan*
[d]*Advanced Institute for Materials Research (WPI-AIMR), Tohoku University, 2-1-1 Katahira, Aoba-ku, Sendai 980-8577, Japan*

systematic investigation into how nanometer-scale structural modulation at the Cu–Ag interface affects *CO transport and governs product selectivity. To the best of our knowledge, this is the first study to systematically examine eCO_2R selectivity in a flow cell configuration using Cu–Ag layered catalysts with nanometer-controlled Ag thickness.

Results and discussion

Catalyst preparation and structural characterization

Cu–Ag TEs with varying Ag layer thicknesses were prepared, along with Cu and Ag single-metal electrodes as references (see SI for details). The electrodes were fabricated by sequentially depositing Cu and then Ag onto a porous PTFE membrane. The prepared tandem electrodes with a fixed Cu layer thickness of 150 nm and Ag layers of 0.9–150 nm are denoted as Cu*X*Ag, where *X* is the Ag thickness (nm). The thicknesses of the deposited Cu and Ag layers were monitored by a quartz crystal microbalance during deposition, and the thickness profiles are provided in Fig. S1. For comparison, Cu and Ag electrodes, each with a thickness of 150 nm, were also prepared and are simply denoted as Cu and Ag, respectively.

To investigate the interface structure, cross-sectional and top-view scanning electron microscopy (SEM) analyses were conducted on Cu150Ag. The cross-sectional SEM image revealed two distinct layers on the PTFE substrate: a dark lower layer and a bright upper layer (Fig. 1a). These layers correspond to Cu and Ag, respectively, demonstrating the successful formation of the heterostructure. A SEM top-view revealed a densely packed granular surface with lateral feature sizes on the order of several tens of nanometers (Fig. 1b). Energy-dispersive X-ray spectroscopy

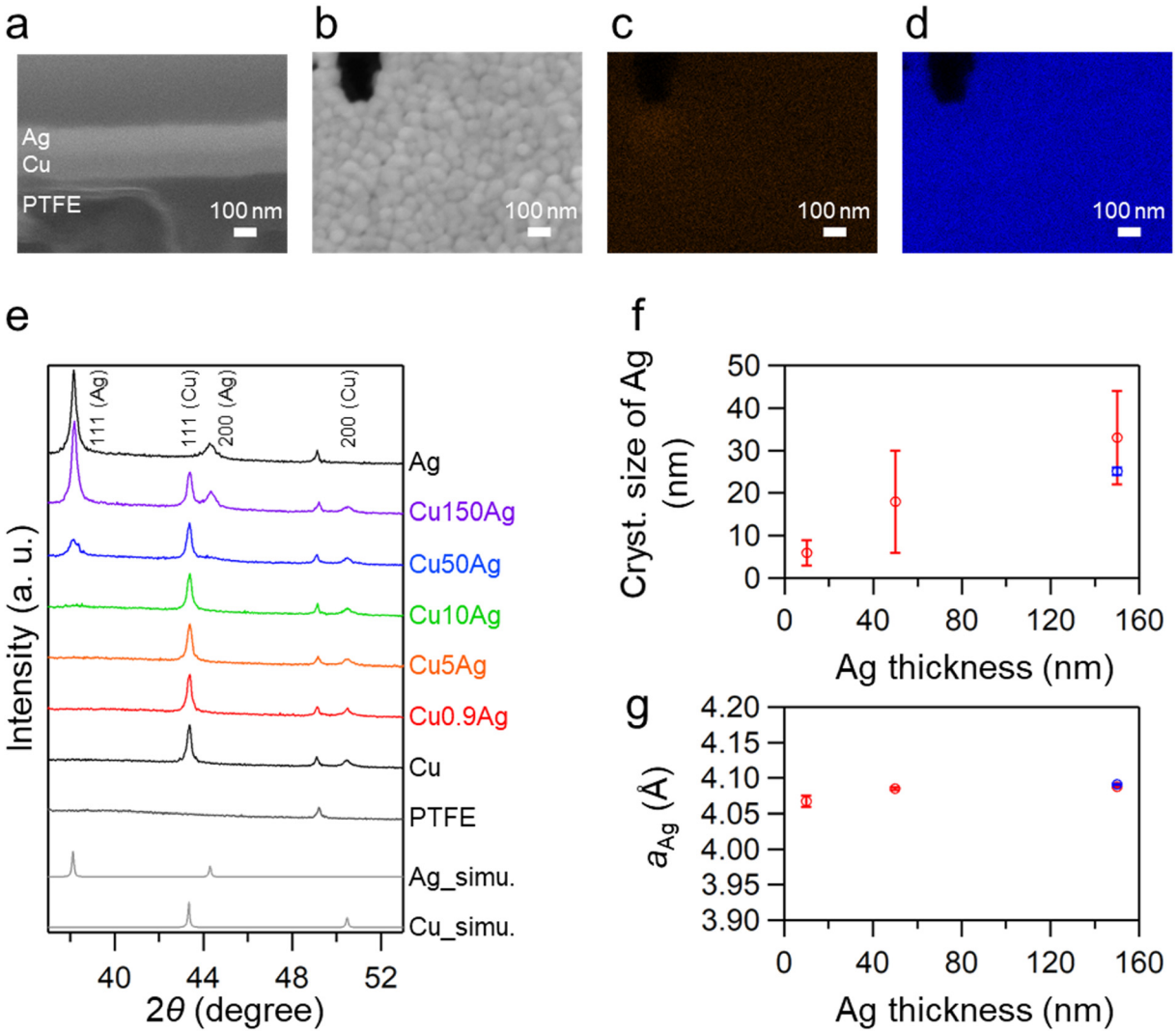

Fig. 1 (a) Cross-sectional SEM image of Cu150Ag. (b–d) Top-view SEM and EDS elemental maps of Cu150Ag for (c) Cu and (d) Ag. (e) XRD patterns of Cu, Ag, Cu–Ag TEs, and PTFE membrane. Simulated reference patterns of Cu and Ag are based on reported crystallographic data.[21] (f and g) Ag overlayer thickness dependence of Ag crystallite size (f) and lattice constant (g), calculated by Rietveld refinement: Cu–Ag TEs (red circles) and Ag (blue circle).

(EDS) mapping showed homogeneous distributions of both Cu and Ag signals (Fig. 1c and d), which could indicate partial surface exposure of Cu. This surface exposure of Cu was revealed by *in situ* Raman spectroscopy, which detected peaks assignable to copper oxide species (Fig. S2).

X-ray diffraction (XRD) measurements were performed to examine the electrode structures. Cu and Ag exhibited diffraction patterns consistent with the face-centered cubic (fcc) structure, along with a characteristic peak from the PTFE membrane at 2θ = 49° (Fig. 1e). In Cu–Ag TEs, Cu diffraction peaks were observed at all Ag thicknesses, whereas Ag peaks became discernible only when the Ag layer exceeded 10 nm. The intensity of the Ag(111) peak increased with increasing Ag thickness, indicating growth of the Ag phase. Rietveld refinement further confirmed that the Ag crystallite size increased with layer thickness (Fig. 1f). The Ag lattice constant varied slightly with thickness, increasing by 0.021 Å (0.5%) from 10 to 150 nm (Fig. 1g).

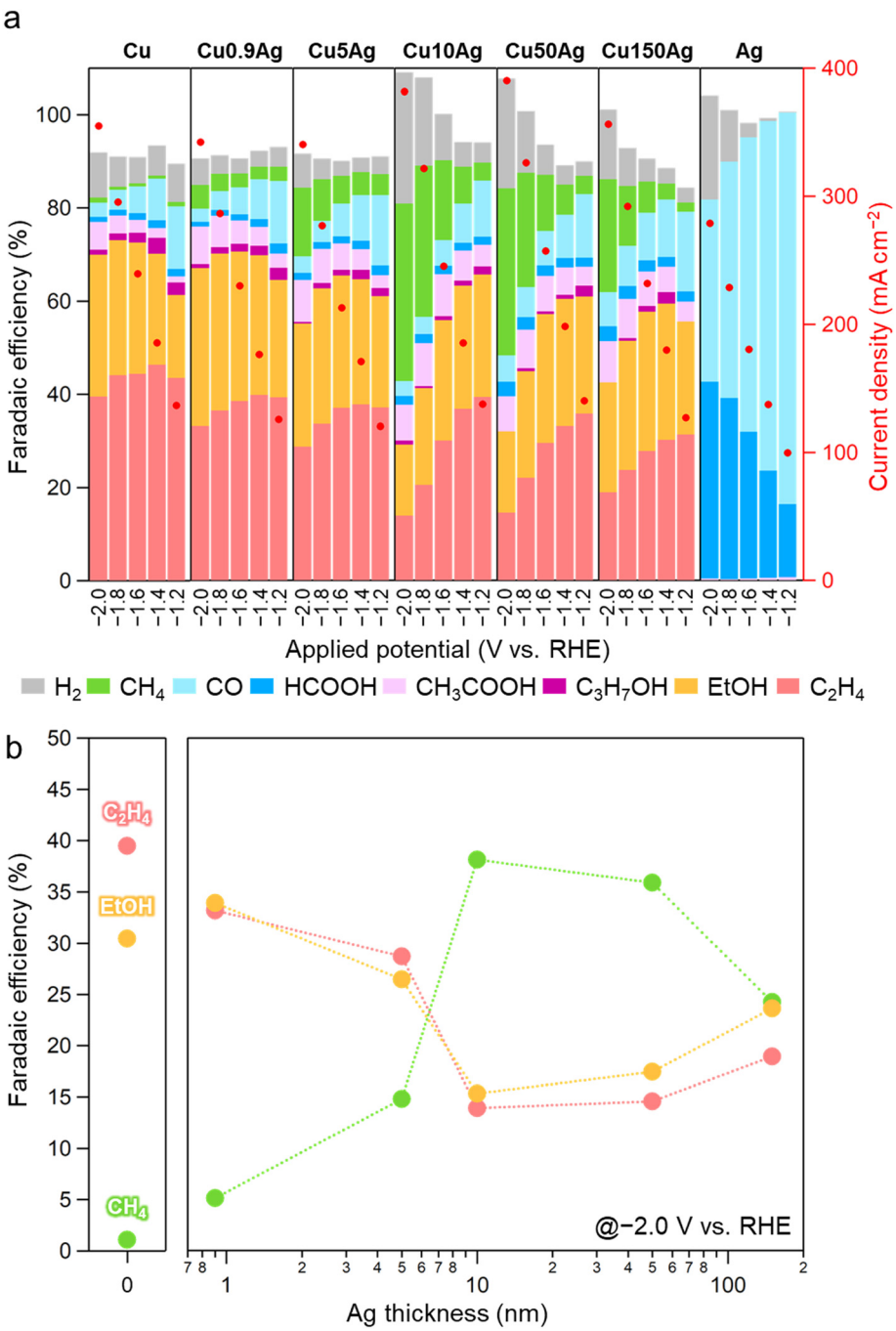

Fig. 2 Product distributions on Cu, Ag, and Cu–Ag TEs. (a) faradaic efficiencies for all products (left axis) and current densities (red circles, right axis). (b) $FE_{C_2H_4}$ (red), FE_{EtOH} (orange), and FE_{CH_4} (green) at −2.0 V *vs.* RHE as a function of Ag overlayer thickness. Dotted lines are guides for the eye.

Electrochemical CO_2 reduction performance

The electrochemical CO_2 reduction (eCO_2R) performance of the electrodes was evaluated using chronoamperometry in a flow cell. Cu predominantly generated C_{2+} over the entire potential range, with EtOH and C_2H_4 as the main products (Fig. 2a). In contrast, Ag mainly produced CO, particularly at less negative potentials. As the applied potential became more negative, the faradaic efficiency for CO (FE_{CO}) decreased, whereas those for formic acid (HCOOH) and hydrogen (H_2) increased (see SI for the definition of faradaic efficiency).

Cu–Ag TEs exhibited a marked enhancement in the faradaic efficiency for CH_4 (FE_{CH_4}) compared to both Cu and Ag, which showed FE_{CH_4} less than 2%. To evaluate the impact of Ag layer thickness on product distribution, we examined the thickness-dependent FE_{EtOH}, $FE_{C_2H_4}$, and FE_{CH_4} at −2.0 V *vs.* RHE (Fig. 2b).

The amount of FE_{CH_4} increased with increasing Ag thickness, peaking at Cu10Ag where CH_4 became the dominant product. At Ag thicknesses of 50 nm and above, CH_4 remained the major product (Cu50Ag and Cu150Ag), but FE_{CH_4} gradually declined with increasing Ag thickness. Concurrently, FE_{EtOH} and $FE_{C_2H_4}$ decreased from Cu0.9Ag to Cu10Ag, consistent with a shift toward CH_4 formation. At thicker Ag layers (Cu50Ag and Cu150Ag), both of FE_{EtOH} and $FE_{C_2H_4}$ partially recovered. Among all Cu–Ag TEs, Cu0.9Ag exhibited the highest FE_{EtOH} and exceeded that of Cu. This non-monotonic behavior highlights the intricate interplay between Ag layer thickness and product selectivity in the Cu–Ag tandem system.

To rule out possible effects of the total electrode thickness, we evaluated thickness-matched Cu electrodes (Cu–Cu electrodes) with total Cu thicknesses of 150.9 (150 + 0.9), 160 (150 + 10), and 300 (150 + 150) nm as controls. As shown in Fig. S3 and S4, varying the Cu thickness alone did not reproduce the selectivity tuning observed in the Cu–Ag TEs.

In situ Raman spectroscopy

To gain mechanistic insights into the observed trends in product selectivity, we conducted *in situ* Raman spectroscopy under eCO_2R conditions using a flow cell (se SI for details). Raman spectra were collected at open-circuit potential (OCP) and during chronopotentiometry in the current density range of 10–90 mA cm^{-2}. Across all Cu–Ag TEs, Raman peaks attributed to copper oxides[22,23] were observed at OCP, confirming partial surface exposure of Cu (Fig. 3a and S2).

In the low-wavenumber region (240–1400 cm^{-1}), Cu exhibited a characteristic Cu–*CO peak at ~370 cm^{-1},[22,24] whereas no such features were detected on Cu–Ag TEs. In the high-wavenumber region (1400–2200 cm^{-1}), Cu showed a Raman peak at 1520–1550 cm^{-1}, assignable to asymmetric stretching of adsorbed CO_2^- (ref. 25; Fig. 3b). Meanwhile, on Cu–Ag TEs except for Cu0.9Ag, we observed a peak near 1604 cm^{-1}, which is attributed to the formation of $*CH_x$–*CO.[17] Previous studies

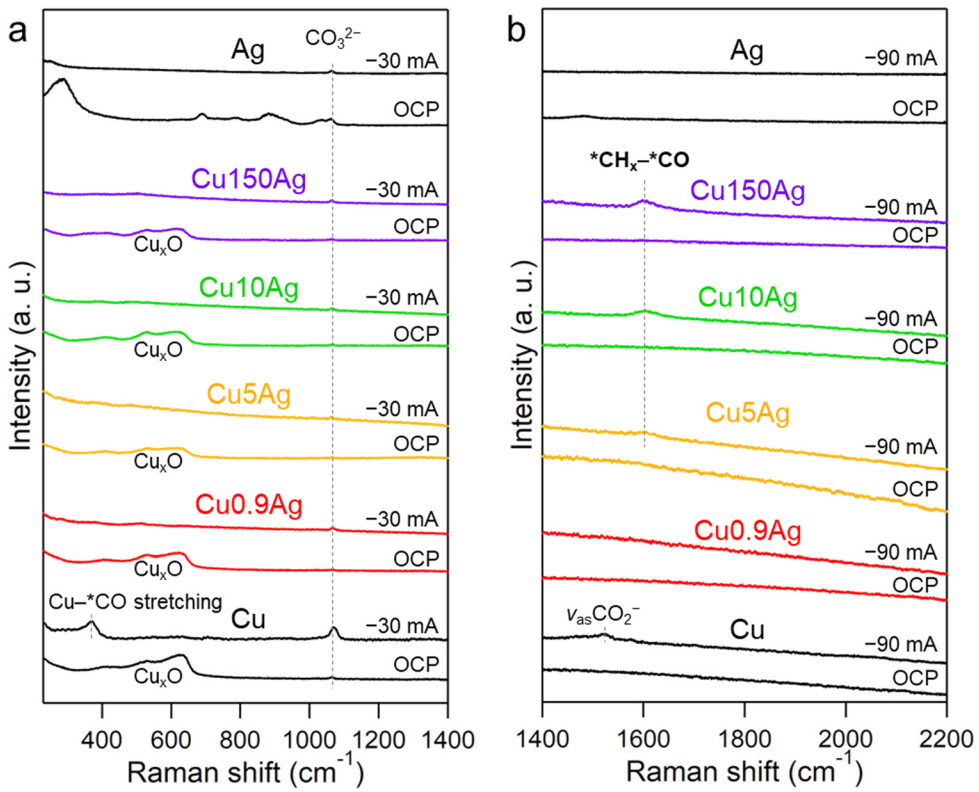

Fig. 3 *In situ* Raman spectra of Cu, Ag and Cu–Ag TEs in the (a) low-wavenumber region and (b) high-wavenumber region at OCP and under various applied currents.

have suggested that *CH_x–*CO coupling between *CH_x formed on Cu and *CO supplied from Ag promotes ethanol formation over ethylene.[17,18,26] DFT calculations in those studies indicate that the resulting *CH_xCO intermediates are preferentially reduced into ethanol, especially on Cu(111)-oriented surfaces.[17,18] Recent spectroscopic, theoretical, and data-driven studies have further highlighted asymmetric *CH_x–*CO[27] and *CHO–*CH_x[28] coupling as key C–C coupling motifs for C_{2+} formation. Taken together, the emergence of *CH_x–*CO Raman peak, the increased EtOH/(EtOH + C_2H_4) ratios relative to Cu (Fig. S5), and mechanistic insights from prior studies indicate that *CH_x–*CO pathways are promoted on Cu–Ag TEs.

Notably, the absence of Cu–*CO on Cu–Ag TEs implies that the *CO rapidly converts into downstream intermediates, preventing its accumulation on the TEs. The absence of the 1604 cm^{-1} peak for Cu0.9Ag is likely due to rapid CO turnover at the interface, resulting in a low steady-state population of CO-involving intermediates below the Raman detection limit. Similarly, the absence of *CH_x signals at around 1435 cm^{-1} (ref. 17, 29 and 30) in both Cu and Cu–Ag TEs suggests that these intermediates are rapidly consumed *via* coupling with *CO or *H. This indicates high surface turnover and low steady-state coverage of *CH_x species. These spectroscopic observations indicate the involvement of *CH_x–*CO-related intermediates and rapid *CO turnover on Cu–Ag TEs.

Guided by these insights, we next develop a competition model between *CH_x–*CO and *CH_x–*H coupling to account for the observed thickness-dependent selectivity.

Ag layer thickness-dependent product selectivity

The thickness dependence of faradaic efficiency on Cu–Ag TEs (Fig. 2b) indicates a competitive relationship between the production of CH_4 and C_{2+}, governed by whether *CH_x couples with *H (leading to CH_4) or with *CO (leading to C_{2+}). Fig. S6 clearly shows simultaneous increase in FE_{CH_4} and FE_{H_2} as the Ag layer thickness increases, which implies that CH_4 formation is promoted by *CH_x–*H coupling.[31] This pathway is likely facilitated by an increase in surface *H coverage, originating from the enhanced HER. Under these conditions, *H intermediates may compete with *CO for coupling with *CH_x, thereby shifting the reaction pathway toward CH_4 formation.

The competition between *CH_x–*H and *CH_x–*CO pathways is further modulated by the Ag layer thickness, which influences the geometrical configuration of the Cu–Ag interface. As revealed by Rietveld refinement (Fig. 1f), increasing the Ag layer thickness results in the growth of Ag crystallites, suggesting a coarsening of Ag grains. Based on the crystallite-

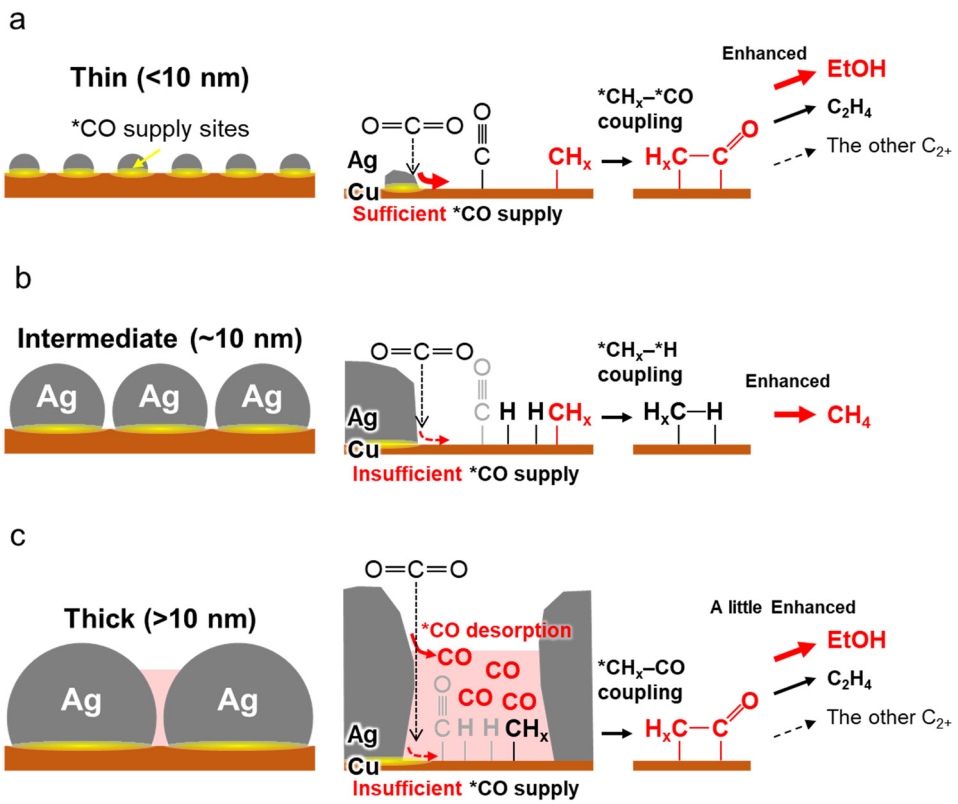

Fig. 4 Schematic illustrations of Cu–Ag interfacial environments and plausible reaction pathways: (a) low Ag thicknesses (<10 nm); small grains generate a large interfacial perimeter, enabling *CO spillover and promoting *CH_x–*CO coupling toward C_{2+}. (b) Intermediate thickness (~10 nm); decreased perimeter and increased *H coverage favor *CH_x–*H coupling toward CH_4 selectivity. (c) Higher thicknesses (>10 nm); limited *CO spillover leads to *CO desorption and simultaneous CO accumulation on the Cu surface, promoting *CH_x–CO (an Eley–Rideal pathway) toward C_{2+} production.

size trend, we obtained a semi-quantitative, XRD-based estimate of the total Cu–Ag interfacial perimeter per geometric area as a function of Ag thickness (Table S1 and Fig. S7). The estimate indicates that the total Cu–Ag interfacial perimeter decreases with increasing Ag thickness for samples where the crystallite size could be determined (≥10 nm).

At small Ag thicknesses (Cu0.9Ag and Cu5Ag), the Ag layer tends to consist of fine grains, resulting in a large total interfacial perimeter between Cu and Ag due to numerous small Cu–Ag contact regions. This extensive interface likely facilitates effective *CO spillover from Ag to Cu, thereby promoting $*CH_x$–*CO coupling and favoring the formation of C_{2+} such as EtOH and C_2H_4 (Fig. 4a). As the Ag layer becomes thicker (Fig. 4b), the Ag grains coarsen and individual Cu–Ag interfacial regions grow larger, thereby reducing the total number of interfacial regions and the overall interfacial perimeter. This structural evolution decreases the total perimeter of Cu–Ag interface available for *CO transfer, resulting in diminished *CO availability at Cu sites. Consequently, $*CH_x$ intermediates are more likely to couple with *H rather than *CO, shifting the selectivity toward CH_4 formation (Fig. 4b). The CH_4 selectivity peaked at Cu10Ag, where both limited *CO spillover and elevated *H coverage synergistically favored the $*CH_x$–*H pathway.

Notably, at higher Ag thicknesses (Cu50Ag and Cu150Ag), FE_{CH_4} declined, whereas EtOH and C_2H_4 formation partially recovered (Fig. 2b). This behavior coincided with an increase in CO production (Fig. S8), indicating the accumulation of CO near the Cu surface. This accumulation likely arises from desorption of *CO that is unable to spill over to Cu due to the reduced interfacial perimeter caused by grain coarsening. The resulting CO-rich local environment may enable $*CH_x$–CO coupling *via* an Eley–Rideal mechanism,[17] potentially contributing to the observed resurgence of C_{2+} (Fig. 4c).

Conclusion

In this study, we prepared Cu–Ag TEs with nanometer-controlled Ag overlayer thicknesses to systematically investigate the impact of interfacial structure on eCO_2R selectivity. Electrochemical performance tests revealed that CH_4 formation, which was scarcely observed on either Cu or Ag alone, was substantially promoted on Cu–Ag TEs. faradaic efficiency trends indicated a competitive relationship between the formation of CH_4 and C_{2+} (mainly EtOH and C_2H_4): CH_4 selectivity peaked at an Ag thickness of 10 nm, whereas C_{2+} selectivity decreased up to this point and subsequently recovered at higher thicknesses.

Detailed structural and spectroscopic analyses figured out the origins for the non-monotonic behavior of the product selectivity on Cu–Ag TEs, which is sensitively modulated by the Ag layer thickness. Based on these findings, we could propose the plausible reaction pathways in the catalytic environments of the Cu–Ag interlayer spaces. At low Ag thicknesses, small Ag grains yield a large total interfacial perimeter, enabling efficient *CO spillover to the Cu surface and promoting $*CH_x$–*CO coupling. As the Ag layer thickens, grain coarsening reduces the total Cu–Ag interfacial perimeter, diminishing *CO supply and favoring $*CH_x$–*H coupling. At higher thicknesses, local CO accumulation on the Cu surface may enable an additional $*CH_x$–CO coupling route *via* an Eley–Rideal mechanism, contributing to the resurgence of C_{2+}.

This work establishes a versatile tandem catalyst platform that can operate under flow cell conditions, and also provides nanometer-scale mechanistic insights that can inform the rational design of highly efficient eCO_2R catalysts. More broadly, beyond efficiency, data-driven approaches may accelerate the exploration of complex electrocatalyst design spaces where stability and durability are equally critical, including multicomponent alloy systems.[32,33]

Conflicts of interest

There are no conflicts to declare.

Data availability

All experimental data, including electrochemical measurements and *in situ* Raman spectra, are available within the article and its supplementary information (SI). The SI is available at DOI: https://doi.org/10.1039/d5nr04783h.

Additional data are available from the corresponding author upon reasonable request.

Acknowledgements

The authors acknowledge funding from Japan Society for the Promotion of Science Grants-in-Aid for Scientific Research (23H00313, 24H02202, 24H02205) and Moonshot Research and Development Program (JPNP18016).

References

1 A. Bagger, W. Ju, A. S. Varela, P. Strasser and J. Rossmeisl, *ChemPhysChem*, 2017, **18**, 3266–3273.
2 Y. Y. Birdja, E. Pérez-Gallent, M. C. Figueiredo, A. J. Göttle, F. Calle-Vallejo and M. T. M. Koper, *Nat. Energy*, 2019, **4**, 732–745.
3 P. De Luna, C. Hahn, D. Higgins, S. A. Jaffer, T. F. Jaramillo and E. H. Sargent, *Science*, 2019, **364**, eaav3506.
4 Y. Hori, H. Wakebe, T. Tsukamoto and O. Koga, *Electrochim. Acta*, 1994, **39**, 1833–1839.
5 Y. Hori, I. Takahashi, O. Koga and N. Hoshi, *J. Phys. Chem. B*, 2002, **106**, 15–17.
6 S. Nitopi, E. Bertheussen, S. B. Scott, X. Liu, A. K. Engstfeld, S. Horch, B. Seger, I. E. L. Stephens, K. Chan, C. Hahn, J. K. Nørskov, T. F. Jaramillo and I. Chorkendorff, *Chem. Rev.*, 2019, **119**, 7610–7672.

7 M. Sun, J. Cheng and M. Yamauchi, *Nat. Commun.*, 2024, **15**, 491.
8 M. Sun, A. Staykov and M. Yamauchi, *ACS Catal.*, 2022, **12**, 14856–14863.
9 B. Cao, F.-Z. Li and J. Gu, *ACS Catal.*, 2022, **12**, 9735–9752.
10 B. Zhang, L. Wang, D. Li, Z. Li, R. Bu and Y. Lu, *Chem Catal.*, 2022, **2**, 3395–3429.
11 X. She, T. Zhang, Z. Li, H. Li, H. Xu and J. Wu, *Cell Rep. Phys. Sci.*, 2020, **1**, 100051.
12 T. Zhang, J. C. Bui, Z. Li, A. T. Bell, A. Z. Weber and J. Wu, *Nat. Catal.*, 2022, **5**, 202–211.
13 C. Chen, Y. Li, S. Yu, S. Louisia, J. Jin, M. Li, M. B. Ross and P. Yang, *Joule*, 2020, **4**, 1688–1699.
14 D. Ren, B. S.-H. Ang and B. S. Yeo, *ACS Catal.*, 2016, **6**, 8239–8247.
15 S. Zhang, S. Zhao, D. Qu, X. Liu, Y. Wu, Y. Chen and W. Huang, *Small*, 2021, **17**, 2102293.
16 A. Herzog, A. Bergmann, H. S. Jeon, J. Timoshenko, S. Kühl, C. Rettenmaier, M. Lopez Luna, F. T. Haase and B. Roldan Cuenya, *Angew. Chem., Int. Ed.*, 2021, **60**, 7426–7435.
17 P. Luan, X. Dong, L. Liu, J. Xiao, P. Zhang, J. Zhang, H. Chi, Q. Wang, C. Ding, R. Li and C. Li, *ACS Catal.*, 2024, **14**, 8776–8785.
18 L. R. L. Ting, O. Piqué, S. Y. Lim, M. Tanhaei, F. Calle-Vallejo and B. S. Yeo, *ACS Catal.*, 2020, **10**, 4059–4069.
19 S. Wang, F. Li, J. Zhao, Y. Zeng, Y. Li, Z.-Y. Lin, T.-J. Lee, S. Liu, X. Ren, W. Wang, Y. Chen, S.-F. Hung, Y.-R. Lu, Y. Cui, X. Yang, X. Li, Y. Huang and B. Liu, *Nat. Commun.*, 2024, **15**, 10247.
20 A. Anzai, M. Higashi and M. Yamauchi, *Chem. Commun.*, 2023, **59**, 11188–11191.
21 I.-K. Suh, H. Ohta and Y. Waseda, *J. Mater. Sci.*, 1988, **23**, 757–760.
22 D. Zhang, X. Liu, Y. Zhao, H. Zhang, A. V. Rudnev and J.-F. Li, *Chem. Sci.*, 2025, **16**, 4916–4936.
23 Y. Jiang, H. Li, C. Chen, Y. Zheng and S.-Z. Qiao, *ACS Catal.*, 2024, **14**, 8310–8316.
24 C. Zhan, F. Dattila, C. Rettenmaier, A. Herzog, M. Herran, T. Wagner, F. Scholten, A. Bergmann, N. López and B. Roldan Cuenya, *Nat. Energy*, 2024, **9**, 1485–1496.
25 I. V. Chernyshova, P. Somasundaran and S. Ponnurangam, *Proc. Natl. Acad. Sci. U. S. A.*, 2018, **115**, E9261–E9270.
26 J. Li, C. Li, J. Hou, W. Gao, X. Chang, Q. Lu and B. Xu, *J. Am. Chem. Soc.*, 2022, **144**, 20495–20506.
27 M. Sun, D. S. R. Rocabado, J. Cheng, T. G. Noguchi, M. Donoshita, T. Matsuu, M. Higashi, T. Fujigaya, T. Ishimoto and M. Yamauchi, *Angew. Chem., Int. Ed.*, 2025, **64**, e202502740.
28 H. Li, X. Li, P. Wang, Z. Zhang, K. Davey, J. Q. Shi and S.-Z. Qiao, *J. Am. Chem. Soc.*, 2024, **146**, 22850–22858.
29 S. L. Wunder, M. I. Bell and G. Zerbi, *J. Chem. Phys.*, 1986, **85**, 3827–3839.
30 R. Mutter, W. Stille and G. Strobl, *J. Polym. Sci., Part B: Polym. Phys.*, 1993, **31**, 99–105.
31 A. Anzai, M. Fukushima, D. S. R. Rocabado, T. Ishimoto, T. Sugiyama, B. Ohtani, H. Kobayashi, M.-H. Liu, M. Donoshita, T. G. Noguchi, S. K. Maurya, K. Kato, C. Y. Sit, P. J. A. Kenis and M. Yamauchi, *ACS Appl. Mater. Interfaces*, 2025, **17**, 22665–22676.
32 Z. Tan, X. Li, R. Bai, C. Guo, X. Han, J. Q. Shi, J. Zhang and H. Li, *ACS Catal.*, 2025, **15**, 13097–13106.
33 B. Zhu, S. Huang, O. Seo, M. Cao, D. Matsumura, H. Gu and D. Wu, *J. Am. Chem. Soc.*, 2025, **147**, 11250–11256.